



Detection of Carbon Monoxide in the Atmosphere of WASP-39b Applying Standard Cross-correlation Techniques to JWST NIRSpec G395H Data

Emma Esparza-Borges^{1,2} , Mercedes López-Morales³ , Jéa I. Adams Redai³ , Enric Pallé^{1,2} , James Kirk⁴ , Núria Casasayas-Barris¹ , Natasha E. Batalha⁵ , Benjamin V. Rackham^{6,7,35} , Jacob L. Bean⁸ , S. L. Casewell⁹ , Leen Decin¹⁰ , Leonardo A. Dos Santos¹¹ , Antonio García Muñoz¹² , Joseph Harrington¹³ , Kevin Heng¹⁴ , Renyu Hu^{15,16} , Luigi Mancini^{17,18,19} , Karan Molaverdikhani^{20,21} , Giuseppe Morello^{1,22} , Nikolay K. Nikolov¹¹ , Matthew C. Nixon²³ , Seth Redfield²⁴ , Kevin B. Stevenson²⁵ , Hannah R. Wakeford²⁶ , Munazza K. Alam²⁷ , Björn Benneke²⁸ , Jasmina Blecic^{29,30} , Nicolas Crouzet³¹ , Tansu Daylan^{32,36} , Julie Inglis¹⁶ , Laura Kreidberg¹⁸ , Dominique J. M. Petit dit de la Roche³³ , and Jake D. Turner^{34,37}

¹ Instituto de Astrofísica de Canarias, E-38200 La Laguna, Tenerife, Spain; emma.esparza.borges@iac.es

² Departamento de Astrofísica, Universidad de La Laguna, E-38206 La Laguna, Tenerife, Spain

³ Center for Astrophysics | Harvard & Smithsonian, 60 Garden St., Cambridge, MA 02138, USA

⁴ Department of Physics, Imperial College London, Prince Consort Road, London SW7 2AZ, UK

⁵ NASA Ames Research Center, Moffett Field, CA 94035, USA

⁶ Department of Earth, Atmospheric and Planetary Sciences, Massachusetts Institute of Technology, 77 Massachusetts Avenue, Cambridge, MA 02139, USA

⁷ Kavli Institute for Astrophysics and Space Research, Massachusetts Institute of Technology, Cambridge, MA 02139, USA

⁸ Department of Astronomy & Astrophysics, University of Chicago, Chicago, IL 60637, USA

⁹ Centre for Exoplanet Research, School of Physics and Astronomy, University of Leicester, University Road, Leicester LE1 7RH, UK

¹⁰ Institute of Astronomy, KU Leuven, Celestijnenlaan 200D, B-3000 Heverlee, Belgium

¹¹ Space Telescope Science Institute, 3700 San Martin Drive, Baltimore, MD 21218, USA

¹² Université Paris-Saclay, Université Paris Cité, CEA, CNRS, AIM, F-91191, Gif-sur-Yvette, France

¹³ Planetary Sciences Group, Department of Physics and Florida Space Institute, University of Central Florida, Orlando, FL, USA

¹⁴ Ludwig Maximilian University of Munich, Faculty of Physics, Germany

¹⁵ Jet Propulsion Laboratory, California Institute of Technology, Pasadena, CA 91109, USA

¹⁶ Division of Geological and Planetary Sciences, California Institute of Technology, Pasadena, CA 91125, USA

¹⁷ Department of Physics, University of Rome "Tor Vergata", Rome, Italy

¹⁸ Max Planck Institute for Astronomy, Heidelberg, Germany

¹⁹ INAF—Turin Astrophysical Observatory, Pino Torinese, Italy

²⁰ Universitäts-Sternwarte, Fakultät für Physik, Ludwig-Maximilians-Universität München, Scheinerstr. 1, D-81679 München, Germany

²¹ Exzellenzcluster 'Origins', Boltzmannstr. 2, D-85748 Garching, Germany

²² Department of Space, Earth and Environment, Chalmers University of Technology, SE-412 96 Gothenburg, Sweden

²³ Department of Astronomy, University of Maryland, College Park, MD, USA

²⁴ Astronomy Department and Van Vleck Observatory, Wesleyan University, Middletown, CT 06459, USA

²⁵ Johns Hopkins APL, Laurel, MD, USA

²⁶ University of Bristol, HH Wills Physics Laboratory, Tyndall Avenue, Bristol, UK

²⁷ Carnegie Earth & Planets Laboratory, 5241 Broad Branch Road NW, Washington, DC 20015, USA

²⁸ Department of Physics and Institute for Research on Exoplanets, Université de Montréal, Montreal, QC, Canada

²⁹ Department of Physics, New York University Abu Dhabi, Abu Dhabi, UAE

³⁰ Center for Astro, Particle and Planetary Physics (CAP3), New York University Abu Dhabi, Abu Dhabi, UAE

³¹ Leiden Observatory, Leiden University, P.O. Box 9513, 2300 RA Leiden, The Netherlands

³² Department of Astrophysical Sciences, Princeton University, 4 Ivy Lane, Princeton, NJ 08544, USA

³³ Département d'Astronomie, Université de Genève, Sauverny, Switzerland

³⁴ Department of Astronomy and Carl Sagan Institute, Cornell University, Ithaca, NY 14853, USA

Received 2023 June 19; revised 2023 August 10; accepted 2023 August 14; published 2023 September 21

Abstract

Carbon monoxide was recently reported in the atmosphere of the hot Jupiter WASP-39b using the NIRSpec PRISM transit observation of this planet, collected as part of the JWST Transiting Exoplanet Community Early Release Science Program. This detection, however, could not be confidently confirmed in the initial analysis of the higher-resolution observations with NIRSpec G395H disperser. Here we confirm the detection of CO in the atmosphere of WASP-39b using the NIRSpec G395H data and cross-correlation techniques. We do this by searching for the CO signal in the unbinned transmission spectrum of the planet between 4.6 and 5.0 μm , where the contribution of CO is expected to be higher than that of other anticipated molecules in the planet's atmosphere. Our search results in a detection of CO with a cross-correlation function (CCF) significance of 6.6σ when using a template with only $^{12}\text{C}^{16}\text{O}$ lines. The CCF significance of the CO signal increases to 7.5σ when including in the template lines from additional CO isotopologues, with the largest contribution being from $^{13}\text{C}^{16}\text{O}$. Our results

³⁵ 51 Pegasi b Fellow.

³⁶ LSSTC Catalyst Fellow.

³⁷ NHFP Sagan Fellow.

highlight how cross-correlation techniques can be a powerful tool for unveiling the chemical composition of exoplanetary atmospheres from medium-resolution transmission spectra, including the detection of isotopologues.

Unified Astronomy Thesaurus concepts: Exoplanet atmospheres (487); Exoplanet atmospheric composition (2021); Hot Jupiters (753); Astronomical methods (1043)

Supporting material: machine-readable table

1. Introduction

The detection of carbon monoxide (CO) and water (H_2O) in gas giant exoplanet atmospheres has long been regarded as key to understanding how these objects form. From atmospheric CO and H_2O measurements it is possible to estimate the planets carbon-to-oxygen (C/O) ratios. The observed C/O ratios can then help trace the location in the stellar protoplanetary disk where the planets formed, and how they accreted the solids and gas that compose their cores and their atmospheres (see, e.g., Öberg et al. 2011; Mordasini et al. 2016; Madhusudhan et al. 2017; Crispell et al. 2019). Isotopologue ratios have also been suggested as good tracers of planet formation conditions and atmospheric evolution (e.g., Clayton & Nittler 2004; Mollière & Snellen 2019).

H_2O has been readily detectable in planetary atmospheres for years, given the Hubble Space Telescope’s capacity to observe one of its main bands centered around $1.4\ \mu m$ (e.g., Deming et al. 2013; Crouzet et al. 2014; Wakeford et al. 2018; Benneke et al. 2019). CO, on the other hand, has been harder to detect because of the lack of suitable space-based instrumentation targeting the spectral ranges of interest. Nevertheless, a few detections have been possible from the ground for exoplanets around very bright stars, using high-resolution observations ($R \sim 30,000$ – $100,000$) centered on the CO $2.3\ \mu m$ band (e.g., Snellen et al. 2010; Rodler et al. 2012; Brogi et al. 2012; de Kok et al. 2013; Brogi et al. 2014; van Sluijs et al. 2023), and for young exoplanets via direct imaging (e.g., Konopacky et al. 2013; Barman et al. 2015; Petit dit de la Roche, Hoeijmakers, & Snellen 2018). Recent studies have also reported $^{12}C^{16}O/^{13}C^{16}O$ ratios in the atmospheres of a young accreting super-Jupiter (Zhang et al. 2021b) and a brown dwarf (Zhang et al. 2021a), using high-resolution observations centered on the CO $2.3\ \mu m$ band.

With the successful launch of JWST, it is now possible to observe the CO band at $2.3\ \mu m$ and its fundamental band centered at $4.7\ \mu m$ with several of JWST’s onboard instruments. This, combined with JWST’s capacity to observe fainter targets than previous missions could, opens the possibility to search for CO in a large number of exoplanets, enabling future composition population studies.

Early JWST observations have already produced detections of CO in exoplanetary atmospheres. Specifically, Miles et al. (2023) detected the 2.3 and $4.7\ \mu m$ CO bands in the young, directly imaged gas giant planet VHS 1256-1257 b using the NIRSpec IFU setup, and Rustamkulov et al. (2023) reported a detection of CO at $4.7\ \mu m$ in the transiting gas giant exoplanet WASP-39b using NIRSpec PRISM³⁸ ($R \sim 20$ – 300). This last CO detection could not be confirmed by the initial analysis of the observations of WASP-39b with NIRSpec G395H³⁹ (Alderson et al. 2023), although a more recent analysis by Grant et al. (2023) has detected CO in these data using a new

technique that searches for the CO signal in predefined sets of wavelength subbands.

WASP-39b (Faedi et al. 2011) is a $0.28\ M_{Jup}$, $1.27\ R_{Jup}$ exoplanet with an equilibrium temperature of about $1200\ K$, orbiting a G7 V star. Four transits of WASP-39b were observed as part of the JWST Director’s Discretionary Time Transiting Exoplanet Community Early Release Science Program (ERS-1366 PI: N. Batalha; Stevenson et al. 2016; Bean et al. 2018) with the NIRSpec PRISM and G395H, NIRCam WFSS (Wide Field Slitless Spectroscopy), and NIRISS SOSS (Single Object Slitless Spectroscopy) instrument modes, which combined detected a number of chemical species, including Na (19σ), H_2O (33σ), CO_2 (28σ), CO (7σ) (Rustamkulov et al. 2023; Alderson et al. 2023; Ahrer et al. 2023; Feinstein et al. 2023), and the unexpected photochemical byproduct SO_2 (4.8σ ; Tsai et al. 2023; Alderson et al. 2023). The detection of CO and CO_2 , combined with the absence of CH_4 in the transmission spectrum of WASP-39b, reveals that the planet has a supersolar metallicity.

Here we set out to confirm the detections of CO in Rustamkulov et al. (2023) and Grant et al. (2023) and search for CO isotopologues using the JWST Transiting Exoplanet Community Early Release Science (JTEC ERS) Program NIRSpec G395H data set and cross-correlation techniques. Cross-correlation techniques have been ubiquitously used in astronomy for decades (e.g., Tonry & Davis 1979), but they have only been used for exoplanet atmospheres studies through transmission spectroscopy at high ($R \sim 100,000$) resolutions (e.g., Snellen et al. 2010) or direct imaging at medium ($R \sim 1000$) resolutions (e.g., Konopacky et al. 2013). The superb stability and data quality of JWST observations allows us to apply this technique to medium-resolution transmission spectra.

2. Observations and Data Reduction

JWST observed a full transit of WASP-39b with the NIRSpec G395H mode (Jakobsen et al. 2022; Birkmann et al. 2022) as part of the JTEC ERS Program. The target was monitored for 8 hr and 36 minutes between 2022 July 30 21:45 and 2022 July 31 06:21 UTC, using the Bright Object Time Series mode, with the $1.^{\prime\prime}6 \times 1.^{\prime\prime}6$ slit, SUB2048 subarray, and the NRSRAPID readout pattern. The observation resulted in a total of 465 integrations, with 70 groups per integration, with the spectra of the target dispersed across the NRS1 and NRS2 detectors. A particular feature of this data set is a *tilt event* that produced a midtransit jump in flux (see Alderson et al. 2023, for details).

We reduced the NRS1 and NRS2 spectra separately using the Tiberius pipeline (Kirk et al. 2017, 2018, 2019, 2021), but here we focus on the NRS2 detector, which covers the CO fundamental band. Tiberius works from the group-level 2D *rateints* images produced by the STScI Science Calibration Pipeline (Rigby et al. 2023, v1.6.2), from which we remove the *1/f noise* contributions (Jakobsen et al. 2022; Birkmann et al. 2022)

³⁸ Low-resolution ($R \sim 20$ – 300) double-pass prism disperser.

³⁹ High-resolution ($R \sim 2700$) grating disperser.

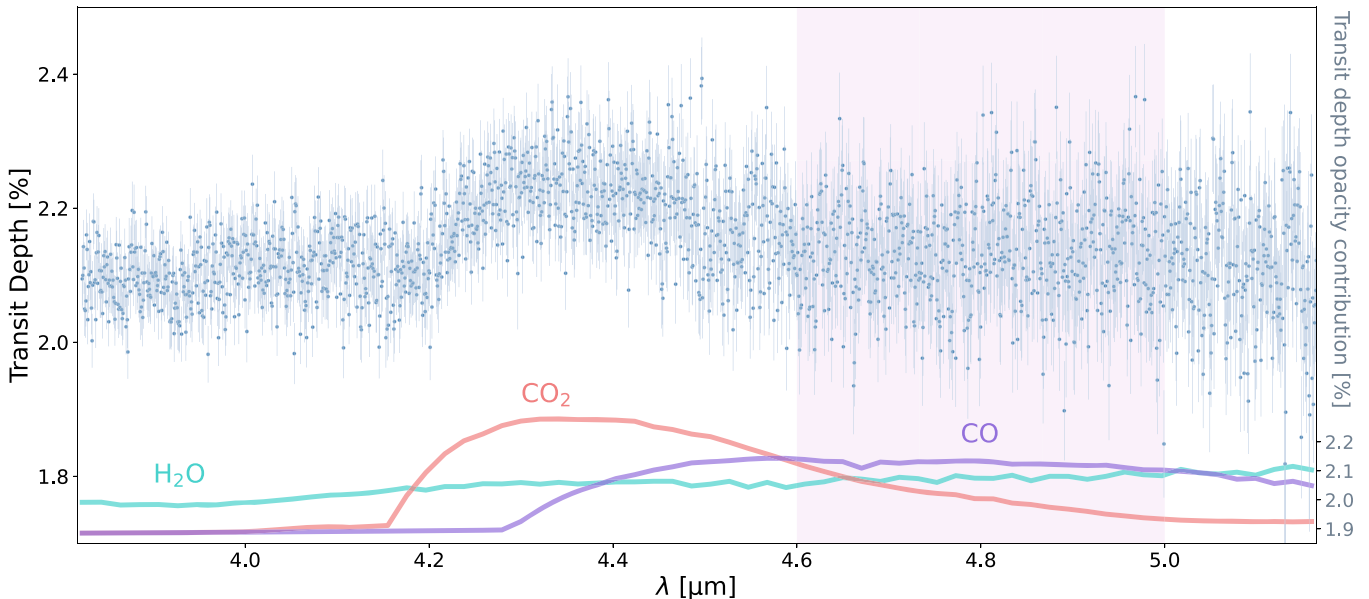


Figure 1. Transmission spectrum of WASP-39b obtained from the JTEC ERS Program NIRSpec G395H NRS2 observation using the Tiberius pipeline. In the lower part of the plot and in the right y-axis, we show the relative opacity contributions of H_2O , CO , and CO_2 , which are the main features expected in that wavelength range. The vertical, purple-shaded area highlights the part of the spectrum where the contribution of CO is expected to be predominant over H_2O and CO_2 . That is the portion of the spectrum used in the CCF analysis.

per column using the median of all off-target pixels in each column. Images were corrected for bad and saturated pixels manually, using custom-made masks that flagged all pixels deviating more than 5σ from running medians along pixel rows and replacing their count values by interpolating the counts from nearby pixels. We traced the spectra fitting Gaussian distributions at each column, and then extracted each spectrum using 4 pixel wide apertures centered on the trace. Residual background flux not captured by the $1/f$ correction was removed by fitting linear polynomials along each column of the detector after masking a 3 pixel-wide region centered on the trace. To remove residual cosmic rays in each stellar spectrum, we compared each spectrum to the median of all the spectra, iteratively removing 8σ or larger outliers and replacing them by linear interpolation with neighboring pixels. Finally, we corrected for any potential wavelength shift in each spectrum by cross-correlating them with the first spectrum and putting all the spectra in a common wavelength grid by linearly resampling them. We used wavelength maps from the JWST Calibration Pipeline to produce the wavelength solution, as in Alderson et al. (2023).

We produced a white light curve (WLC) from the extracted spectra by summing the flux per spectrum over the full wavelength range of the detector ($3.823\text{--}5.177\,\mu\text{m}$), and fitted it with a transit + Gaussian Processes (GP) systematics model using batman (Kreidberg 2015), george (Ambikasaran et al. 2015), and a Monte Carlo Markov Chain (MCMC) implemented using emcee (Foreman-Mackey et al. 2013). The model fitted for the planet-to-star radii ratio (R_p/R_s), orbital inclination (i), epoch of transit (T_0), semimajor axis in units of the stellar radius (a/R_s), the u_1 quadratic law limb-darkening coefficient, and an exponential squared GP kernel with the x - and y -pixel shifts, the FWHM of the spectra, and sky background as parameters. We used a Gaussian prior centered on 0.015 to fit for a/R_s , and uniform priors for all other fitted parameters. For this fit, we kept the orbital period fixed to the value reported by Mancini et al. (2018) and the eccentricity fixed to zero. We fixed the u_2 limb-darkening coefficient to the

Table 1
Wavelength Range per Point, Transit Depth, TD, and Transit Depth Uncertainty, ΔTD , of the WASP-39b Transmission Spectrum Derived using Tiberius

λ_1 (μm)	λ_2 (μm)	TD (ppm)	ΔTD (ppm)
3.822427	3.823099	0.02095	0.00044
3.823099	3.823770	0.02100	0.00045
3.823770	3.824442	0.02143	0.00040
...

(This table is available in its entirety in machine-readable form.)

value computed by ExoTIC-LD for the quadratic limb-darkening law.

For the spectroscopic light curves (SLCs), we generated 2044 light curves at 1 pixel resolution within the NRS2 wavelength range and fitted them using a similar procedure to the one described above, but holding i , T_0 , and a/R_s fixed to the values obtained from the WLC fit, and applied a systematics correction from the WLC fit to aid in fitting the mirror tilt event. We then fitted each spectroscopic light curve using polynomials to describe residual systematics, not GPs. We chose a combination of four linear polynomials describing the change in x -position and y -position of the star on the detector, the FWHM of the stellar trace, and the measured background flux.

Table A1 summarizes the adopted system parameters, the priors for the parameters fitted in the white and spectroscopic light curves, and the posteriors for the WLC fit. Figure 1 shows the obtained transmission spectrum of WASP-39b between $3.823\text{--}5.177\,\mu\text{m}$. The data in the figure are provided in Table 1.

We note that in our analysis we use the spectrum extracted per pixel column, not per resolution element as defined by the Nyquist sampling limit,⁴⁰ since both samplings produce consistent results, but the *per pixel column* sampling is more

⁴⁰ JWST User Documentation (JDoc). Baltimore, MD: Space Telescope Science Institute; <https://jwst-docs.stsci.edu>.

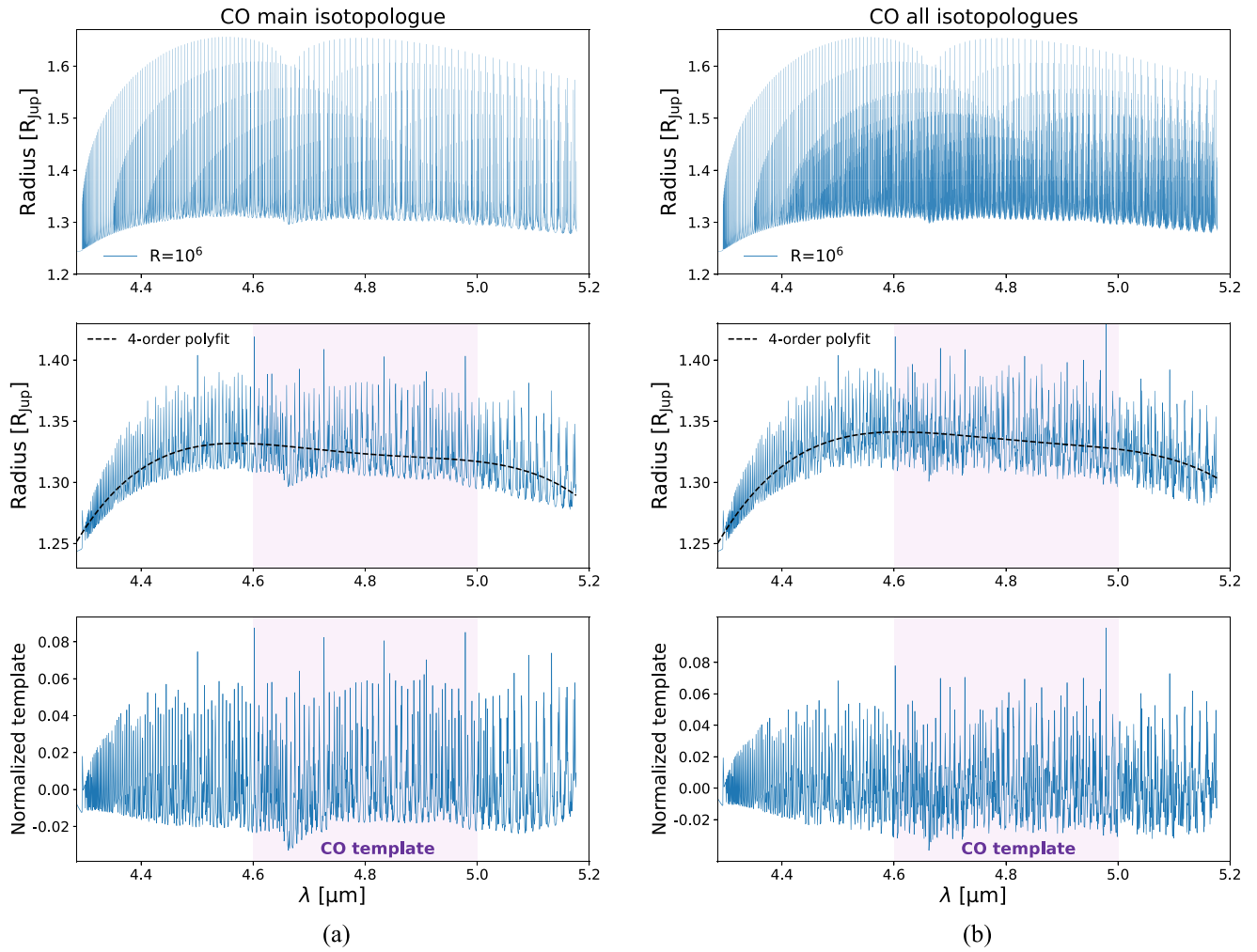


Figure 2. Atmospheric models for the main CO isotopologue (a) and all CO isotopologues (b). Top: high-resolution (10^6) `petitRADTRANS`-computed transmission spectrum model of an atmosphere composed solely of CO. Middle: CO spectrum model degraded to match the resolution of the observed transmission spectrum. The region used for the cross-correlation search is highlighted in purple, with resolving powers of $R = 3470$ and 3803 between 4.6 and $5.0 \mu\text{m}$, respectively. The black dashed line shows the fourth-order polynomial fit that is used for the normalization. Bottom: CO template used in the cross-correlation analysis, calculated by subtracting the fourth-order polynomial fit to the $R = 3470$ – 3803 CO model.

sensitive to the signal of CO and its isotopologues as demonstrated in Appendix B.

3. CO Template Generation

The fundamental band of CO covers air wavelengths between 4.28 and $6.50 \mu\text{m}$. The portion of the band in the rest frame of WASP-39b covered by the NIRSpec NRS2 detector is highlighted by the purple line in Figure 1. For our search, however, we limit the spectral range to 4.6 – $5.0 \mu\text{m}$ to minimize contamination from CO_2 below $4.6 \mu\text{m}$ and H_2O above $5.0 \mu\text{m}$, where the signals from those molecules dominate.

WASP-39 has a barycentric systemic velocity of $-58.4421 \text{ km s}^{-1}$ (Mancini et al. 2018), and the JWST barycentric velocity at the time of the observations was $-28.888 \text{ km s}^{-1}$, as recorded in the image headers under the keyword VELOSYS. Therefore, any atmospheric CO signal from WASP-39b is expected to appear shifted by about $-87.330 \text{ km s}^{-1}$.

We generated pure CO atmospheric transmission spectrum templates of WASP-39b with `petitRADTRANS` (Mollière et al. 2019), using the `lbl` (line-by-line) radiative transfer mode

with a resolving power of $\lambda/\Delta\lambda = 10^6$, and adopting both the main $^{12}\text{C}^{16}\text{O}$ isotopologue and the *all CO isotopes*⁴¹ high-resolution line lists “*CO_main_iso*” and “*CO_all_iso*” from HITEMP (Rothman et al. 2010). For the planet, we adopted a radius of $1.27 R_{\text{Jup}}$, a surface gravity of 407.38 cm s^{-2} following Faedi et al. (2011), an isothermal temperature profile of 1166 K (Mancini et al. 2018), and atmospheric bottom and top pressures of 10^2 and 10^{-12} bars, respectively.

The top panels of Figure 2 show the resultant $R = 10^6$ CO model spectra for the main CO isotopologue (left) and for all CO isotopologues (right). To match the resolution of the observations, we resampled the template CO spectrum produced by `petitRADTRANS` to the sampling of the observations using `spectres`⁴² (Carnall 2017), which produced the spectra shown in the middle panel of Figure 2. The bottom panel of Figure 2 shows the resampled templates, normalized using a fourth-order polynomial fit. The portion of

⁴¹ i.e., $^{12}\text{C}^{16}\text{O}$, $^{13}\text{C}^{16}\text{O}$, $^{12}\text{C}^{18}\text{O}$, $^{12}\text{C}^{17}\text{O}$, $^{13}\text{C}^{18}\text{O}$, and $^{13}\text{C}^{17}\text{O}$ following abundances of 98.65% , 1.11% , 0.20% , $3.7 \times 10^{-2} \%$, $2.2 \times 10^{-3} \%$, and $4.1 \times 10^{-4} \%$, respectively.

⁴² <https://spectres.readthedocs.io/>

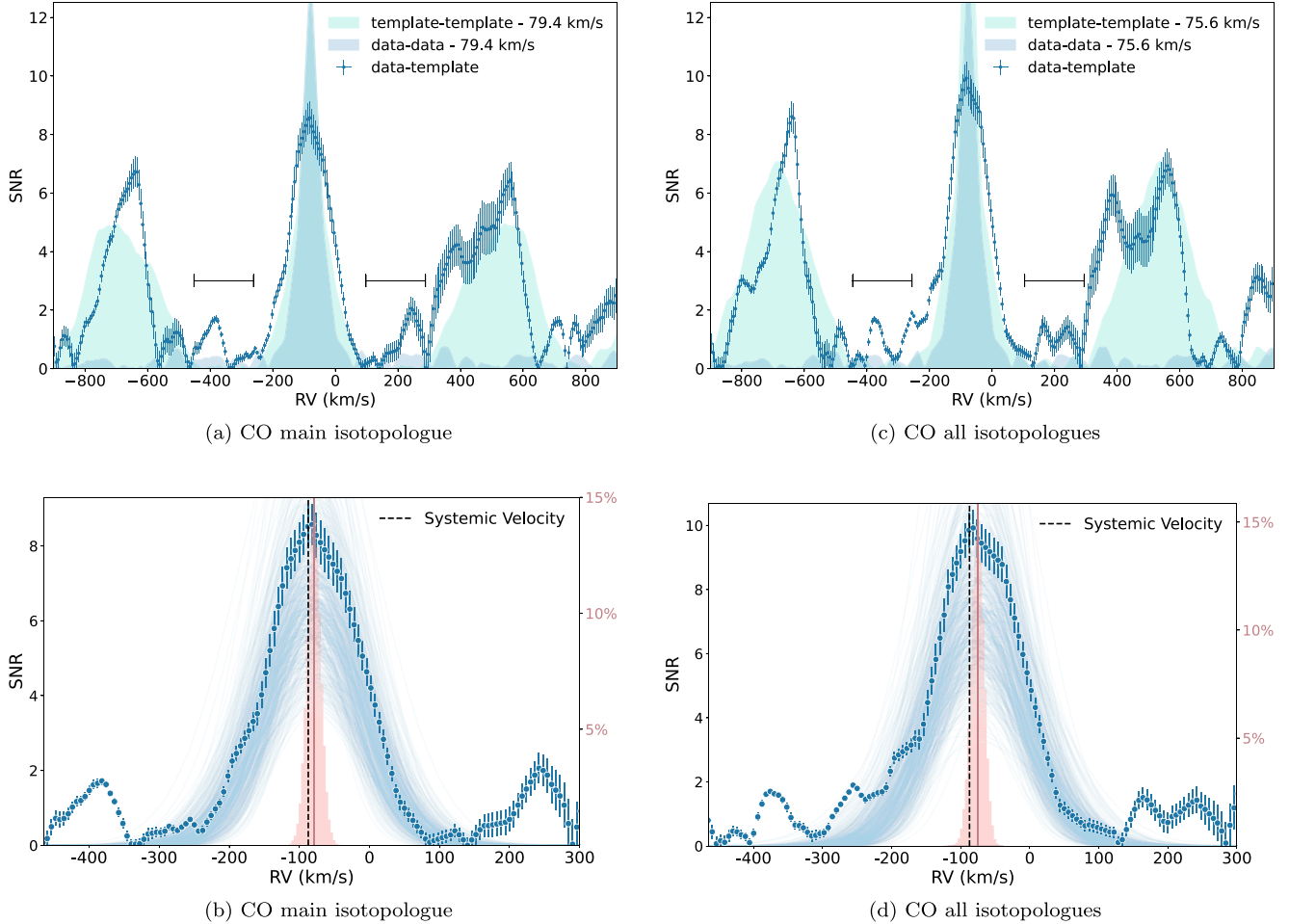


Figure 3. Cross-correlation function (CCF) of the WASP-39b transmission spectrum with the CO main-isotopologue (left panels) and the CO all-isotopologues templates (right panels) in the 4.6–5.0 μm range using a radial-velocity step of 6 km s^{-1} (blue dotted line). The black horizontal bars indicate the continuum regions used to estimate the noise of the CCF, and calculate the significance of the central peak. In panels (a) and (c) we compare the CCFs resulting from the self cross-correlation of the template (light blue area) and the spectrum (dark blue area), which were scaled arbitrarily. Panels (b) and (d) show the central peak of the CCF compared to the histogram of the measurements of the CCF peak radial velocity through random sampling. The right y-axis shows the percentage of samples. The red-continuum line shows the mean value of the RV measurements distribution. The black dashed line shows the systemic velocity relative to the JWST at the time of the observation. The light blue lines show a set of Gaussian fits among the sampled CCFs.

these templates between 4.6 and 5.0 μm , highlighted in purple, is the one used in the cross-correlation search for CO.

As a final step before starting the cross-correlation search, we normalized the observed transmission spectrum of WASP-39b between 4.6 and 5.0 μm by subtracting from the spectrum its mean value in that wavelength range.

4. Cross-correlation Search Results

We carried out cross-correlations between the normalized observed spectrum and the normalized CO main-isotope and CO all-isotopes templates using the *crosscorr* function in PyAstronomy (Czesla et al. 2019),⁴³ shifting the templates with respect to the observed spectrum over a range of systemic velocities between $\pm 1000 \text{ km s}^{-1}$, in 6 km s^{-1} steps, which is about 15 times smaller than the pixel-to-pixel radial-velocity sampling of the spectrum. We also tested the cross-correlation using a smaller, 1 km s^{-1} step, obtaining analogous results. We calculated uncertainties for each correlation value (CV) by propagating the uncertainties in the observed transmission

spectrum of WASP-39b as

$$\Delta\text{CV}(\text{RV}) = \sum_{\lambda} \Delta S(\lambda) T(\text{RV}, \lambda), \quad (1)$$

where $\Delta\text{CV}(\text{RV})$ is the uncertainty of each point of the cross-correlation function (CCF), $\Delta S(\lambda)$ is the uncertainty of each point of the transmission spectrum, and $T(\text{RV}, \lambda)$ is the template used in the cross-correlations at each RV shift.

To put the resulting CVs into more tangible units, we converted the CVs to signal-to-noise ratio (S/N) values as follows: we defined out-of-peak *continuum* regions where the CVs are expected to be dominated by noise. These regions are between $[-452, -262]$ and $[+98, +288] \text{ km s}^{-1}$, defined as 190 km s^{-1} wide regions on each side of the central peak of the CCF, starting at velocities $\pm 3\sigma$ away from that central peak, assuming that the distribution of velocities in the peak is Gaussian; see Figure 3. The conversion of the CVs to S/N values is then calculated as

$$\text{S/N}(\text{per point}) = \frac{|\text{CV}(\text{per point}) - \mu_{\text{cont}}|}{\sigma_{\text{cont}}}, \quad (2)$$

⁴³ <https://github.com/sczesla/PyAstronomy>

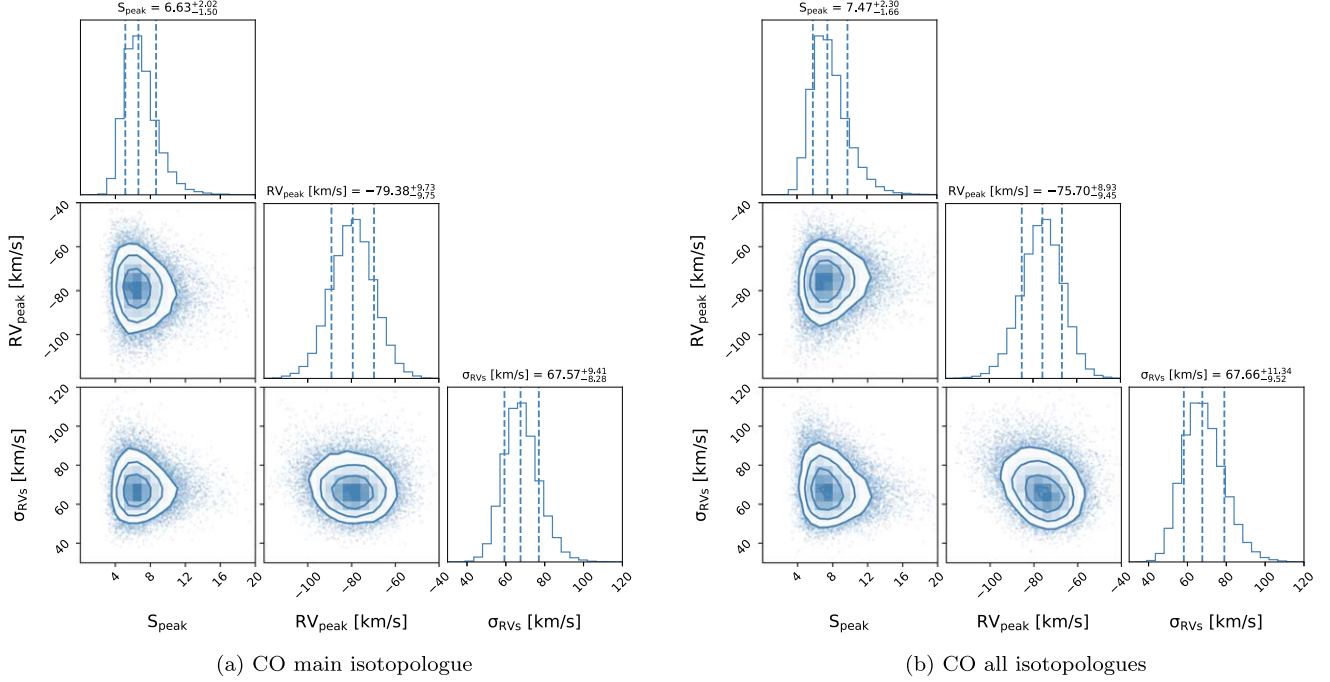


Figure 4. Distribution of the best-fit Gaussian parameters (significance of the central peak, S_{peak} , the central peak velocity, RV_{peak} , and the FWHM of the distribution of velocities, σ_{RVs}) retrieved from the sampled transmission spectra that were randomly generated following a Gaussian distribution centered in the observed transmission spectrum and considering the errors as the Gaussian standard deviation in each point. We performed 30000 iterations. Panels (a) and (b) show the results using the main CO isotopologue and all CO isotopologues templates, respectively.

where μ_{cont} is the mean of the CVs in the continuum regions defined above, and σ_{cont} is the standard deviation of the CVs in those regions.

The resultant CCFs in S/N units are shown in Figure 3, where the continuum regions are indicated by the horizontal black lines in the top panels. The CCFs for the CO main-isotopologue and the CO all-isotopologues templates both show $S/N > 8$ peaks centered near -80 km s^{-1} . This velocity shift is consistent with the barycentric velocity of the system at the time of the observations as discussed in Section 3.

To measure the significance and the actual central velocity of the main peaks in each CCF, we fit a Gaussian to the S/N-converted CCF using the least squares routine `scipy.optimize.curvefit`, and fit for the S/N value of the central peak, S_{peak} , its central velocity, RV_{peak} , and the FWHM of the distribution of velocities, σ_{RVs} .

As a last step, we estimate uncertainties on the values of S_{peak} and RV_{peak} , calculated as described above, by generating 30,000 Monte Carlo random samples of the observed transmission spectrum of WASP-39b in Figure 1, where each point is simulated using a uniform probability distribution of values within the range of errors observed in the spectrum. We then calculate cross-correlations for each simulated spectrum, with each of the two CO templates and measure the significance of the peak and central velocity of each peak as described above. The bottom panels of Figure 3 show the central CCF peaks for each CO template with a sample of the CCFs obtained from individual MCMC realizations in light blue, and the resultant histograms of the central radial velocities of the peak in red. The solid blue lines in the figures correspond to the CCFs obtained from the observed spectrum, and vertical dashed lines correspond to the velocity of the WASP-39 system at the time of the observations. The retrieved distributions of

the three parameters, S_{peak} , RV_{peak} , and σ_{RV} for each CO template are shown in Figure 4.

Our analysis reveals CCF peaks centered at $-79.4 \pm 9.8 \text{ km s}^{-1}$ with a significance of $6.6^{+2.02}_{-1.50} \sigma$ when using the CO main-isotopologue template, and at $-75.7^{+9.2}_{-9.4} \text{ km s}^{-1}$ with a significance of $7.5^{+2.30}_{-1.66} \sigma$ when using the CO all-isotopologues template. Both velocities are consistent within about 1σ with the computed velocity of the system at the time of the observations of -87.33 km s^{-1} . In Appendix C, we show an additional analysis of the observed transmission spectrum using a template composed of the two most abundant CO isotopologues: $^{12}\text{C}^{16}\text{O}$ and $^{13}\text{C}^{16}\text{O}$. The CCF results are similar to the ones obtained using the CO all-isotopologues template. The significance of the detection, being $7.33^{+2.26}_{-1.04} \sigma$, increases compared to the CO main-isotopologue result but is slightly less than the all-isotopologues significance, indicating that the all-isotopologues template produces a better match.

4.1. Secondary Cross-correlation Function Peaks

In addition to the central CCF peaks in agreement with the systemic velocity of WASP-39, the top panels in Figure 3 show secondary CCF peaks at around -600 km s^{-1} and $+600 \text{ km s}^{-1}$, which also appear significant. To elucidate the origin of those peaks, we cross-correlated the observed transmission spectrum of WASP-39b with itself, and each CO template with itself at the same resolution as the observations, over the same range of velocities, $\pm 1000 \text{ km s}^{-1}$, and with the same 6 km s^{-1} steps. The top panels in Figure 3 show the result of the template-to-template CCFs in cyan, and of the data-to-data CCF in light blue. The template-to-template and data-to-data CCFs have been shifted by the RV_{peak} values measured in the previous section so we can compare them directly to the data-to-template CCFs.

The template-to-template CCFs show the expected peak at 0 km s^{-1} , and two symmetric peaks at a mean distance of $\pm 624 \text{ km s}^{-1}$ from the central peak, similar to the ones observed in the data-to-template CCFs. These peaks are expected in the template-to-template CCFs of CO because of the periodic patterns in the distribution of lines in the spectrum of this molecule (see Figure 2). The data-to-data CCF shows the expected peak at 0 km s^{-1} , but no other significant peaks. The presence of the same secondary peaks in the data-to-template and template-to-template CCFs reinforces the conclusion that the signal detected in the transmission spectrum of WASP-39b comes from CO.

5. Conclusions and Discussion

We report the detection of CO in the atmosphere of WASP-39b via a cross-correlation analysis of the JTEC ERS Program NIRSpec G395H data set. Our analysis produces a 6.6σ CCF detection of the fundamental band of CO centered around $4.8 \mu\text{m}$ when using a $^{12}\text{C}^{16}\text{O}$ template and a 7.5σ detection when using a template with all CO isotopologues included in petitRADTRANS.

Our reported detection significance levels are relative to custom-designed baseline regions of the CCF, and as such cannot be readily used to estimate CO abundances. In addition, some stellar CO absorption is expected in WASP-39b's host star, as pointed out by Rustamkulov et al. (2023), and this may dilute the strength of the planetary CO signal, yielding to underestimated detection significances, an effect previously reported by Deming & Sheppard (2017).

Our result confirms the detections of CO in the atmosphere of WASP-39b reported by Rustamkulov et al. (2023) and Grant et al. (2023). This detection, combined with the detection of CO₂ (Team et al. 2023), and the absence of CH₄ (Alderson et al. 2023), reinforces the conclusion of supersolar atmospheric metallicity for this planet (Rustamkulov et al. 2023; Alderson et al. 2023; Ahren et al. 2023; Feinstein et al. 2023; Tsai et al. 2023).

In addition, we show that standard CCF analysis techniques can be used to identify the presence of molecular features in exoplanet atmospheres using transmission spectra with a resolving power of just a few thousand, as is the case of JWST observations in *high-resolution* modes, provided that the spectra are of high-enough quality. CO has the advantage that, at the native resolution of JWST, it still presents a band shape with resolved lines. Still, this technique can be used to search for further molecules in the atmosphere of WASP-39b and also to identify atmospheric molecular species in other planets observed with JWST using these modes.

We highlight the presence of secondary peaks in the CCFs described in Section 4.1, which we also attribute to CO (see Appendix B). Even though we did not exploit the idea in this Letter, it is worth exploring if secondary peaks in CCFs can be

used to increase the confidence of future CO detections, or other molecules, or to place stronger nondetection constraints.

Finally, we highlight how the significance of our CO detection increases from 6.6σ to 7.5σ when adding a number of isotopologues to the $^{12}\text{C}^{16}\text{O}$ template. To evaluate the influence of individual isotopologues, we performed an additional cross-correlation analysis using a $^{12}\text{C}^{16}\text{O}$ (98.7%) + $^{13}\text{C}^{16}\text{O}$ (1.3%) template. In this case the significance of the CCF detection is 7.3σ , indicating that, as expected, $^{13}\text{C}^{16}\text{O}$ is the second most common form of CO. Although the isotopologue detections are admittedly marginal, these results suggest that with future higher signal-to-noise NIRSpec data it will be possible to search for individual isotopologues of CO or other molecules by looking at how the significance of CCF detections increases when adding one isotopologue at a time.

Acknowledgments

This work is based on observations made with the NASA/ESA/CSA JWST. The data were obtained from the Mikulski Archive for Space Telescopes at the Space Telescope Science Institute, which is operated by the Association of Universities for Research in Astronomy, Inc., under NASA contract NAS 5-03127 for JWST. The specific observations can be accessed via doi:[10.17909/gdm2-0q65](https://doi.org/10.17909/gdm2-0q65). These observations are associated with program JWST-ERS-01366. Support for program JWST-ERS-01366 was provided by NASA through a grant from the Space Telescope Science Institute. This work was supported by grant JWST-ERS-01366.033-A. E.E-B and E.P. acknowledge funding from the Spanish Ministry of Economics and Competitiveness through project PGC2018-098153-B-C31. E.E-B acknowledges financial support from the European Union and the State Agency of Investigation of the Spanish Ministry of Science and Innovation (MICINN) under the grant PRE2020-093107 of the Pre-Doc Program for the Training of Doctors (FPI-SO) through FSE funds. J.K. acknowledges financial support from Imperial College London through an Imperial College Research Grant.

Facility: JWST (NIRSpec).

Software: batman (Kreidberg 2015), emcee (Foreman-Mackey et al. 2013), ExoTIC-LD (Grant & Wakeford 2022), george (Ambikasaran et al. 2015), petitRADTRANS (Mollière et al. 2019), PyAstronomy (Czesla et al. 2019, <https://github.com/sczesla/PyAstronomy>), spectres (Carnall 2017), scipy (Virtanen et al. 2020), Tiberius (Kirk et al. 2017, 2018, 2019, 2021).

Appendix A White and Spectroscopic Light Curves Adopted Parameters and Priors

We summarize in Table A1 the adopted system parameters, the priors for the parameters fitted in the white and spectroscopic light curves, and the posteriors for the WLC fit.

Table A1
Adopted Parameters for the White Light Curve (WLC) Fitting, Including Whether the Value Was Fixed in the Fitting or If a Uniform (\mathcal{U}) or Gaussian (\mathcal{G}) Prior Was Used Instead

Parameter	WLC Starting Value ^a	WLC Prior Type	WLC Posterior/SLC Starting Value	SLC Prior Type
P (days)	4.0552941 (34)	Fixed	...	Fixed
e	0	Fixed	...	Fixed
T_0 (BJD)	2,455,342.96913 (63)	$\mathcal{U}(T_0 - 2, T_0 + 2)$	2,459,791.61206 (89)	Fixed
i (deg)	87.32	$\mathcal{U}(80,90)$	$87.81^{+0.20}_{-0.18}$	Fixed
a/R_s	11.55	$\mathcal{G}(11.55, 0.17)$	11.425 ± 0.015	Fixed
R_p/R_s	0.14052	$\mathcal{U}(0., 0.3)$	$0.14636^{+0.00068}_{-0.00071}$	$\mathcal{U}(0., 0.3)$

Note. For uniform priors, the lower and upper bounds are given in brackets. For Gaussian priors, the mean and standard deviation of the priors are given in brackets. We also list the posterior distribution of each parameter after the fitting. The posteriors of the WLC fitting were used as starting values for the spectroscopic light curve (SLC) fitting.

^a Values adopted from Mancini et al. (2018).

Appendix B Spectrum Sampling Tests

To determine whether to use the observed pixel column-sampled or Nyquist limit-sampled spectrum of WASP-39b as input to our CCF analysis in Section 4, we followed the same procedure described in that section, but replacing the observed spectrum of WASP-39b by synthetic spectra.

We generated synthetic CO spectra of WASP-39b following similar steps to the ones described in Section 3. We generated a CO all-isotopologues transmission spectrum of WASP-39b with `petitRADTRANS` (Mollière et al. 2019) at resolving power $R = 10^6$ following as described in Section 3, and then lowered the resolution of the spectrum to match the 1 pixel resolution of our NIRSpec G395H NRS2 observations using the `spectres` module. From that spectrum we produced four different synthetic spectra: 1 pixel sampled; 2 pixel sampled starting on the first pixel of the array, hereafter 2 pixel (0); 2 pixel sampled starting on the second pixel of the array, hereafter 2 pixel (1); and 3 pixel sampled. We normalized each of the synthetic spectra using a fourth-order polynomial, as in Section 3, then selected the portion of the spectrum between 4.6 and 5.0 μm used in our CO search, and added noise using the distribution of noise in the observed spectrum between those wavelengths. As a last step we offset each synthetic

spectrum in wavelength by -87.33 km s^{-1} to match the expected systemic velocity.

We cross-correlated each synthetic spectrum with the CO main-isotopologue and CO all-isotopologues templates described in Section 3, following the same procedure as with the real data described in Section 4. The results are summarized in Figure 5. The figure shows that the CO signal is detected in all cases and with a CCF shape that is very similar to the one produced by the real data, including a main peak centered at the systemic velocity, and secondary peaks at a mean distance of $\pm 624 \text{ km s}^{-1}$ from the central peak. In addition, the S/Ns of the central peaks are consistently larger in the cases when we use the all-isotopologues template, confirming the increase in signal that we see in the real data when we use a template with multiple isotopologues.

The simulations show that 1 pixel sampling produces the same CCF results, but with higher S/N than the other samplings. Therefore we decided to use 1 pixel sampling in our analysis. We note that the peak S/Ns of the CCFs in the simulation are significantly larger than the values obtained in the real data, but we attribute that difference to the simulated spectra only containing CO; in the real data, there are also contributions from H₂O, CO₂, and stellar CO lines (Deming & Sheppard 2017) in that wavelength region, which can dilute the CO signal.

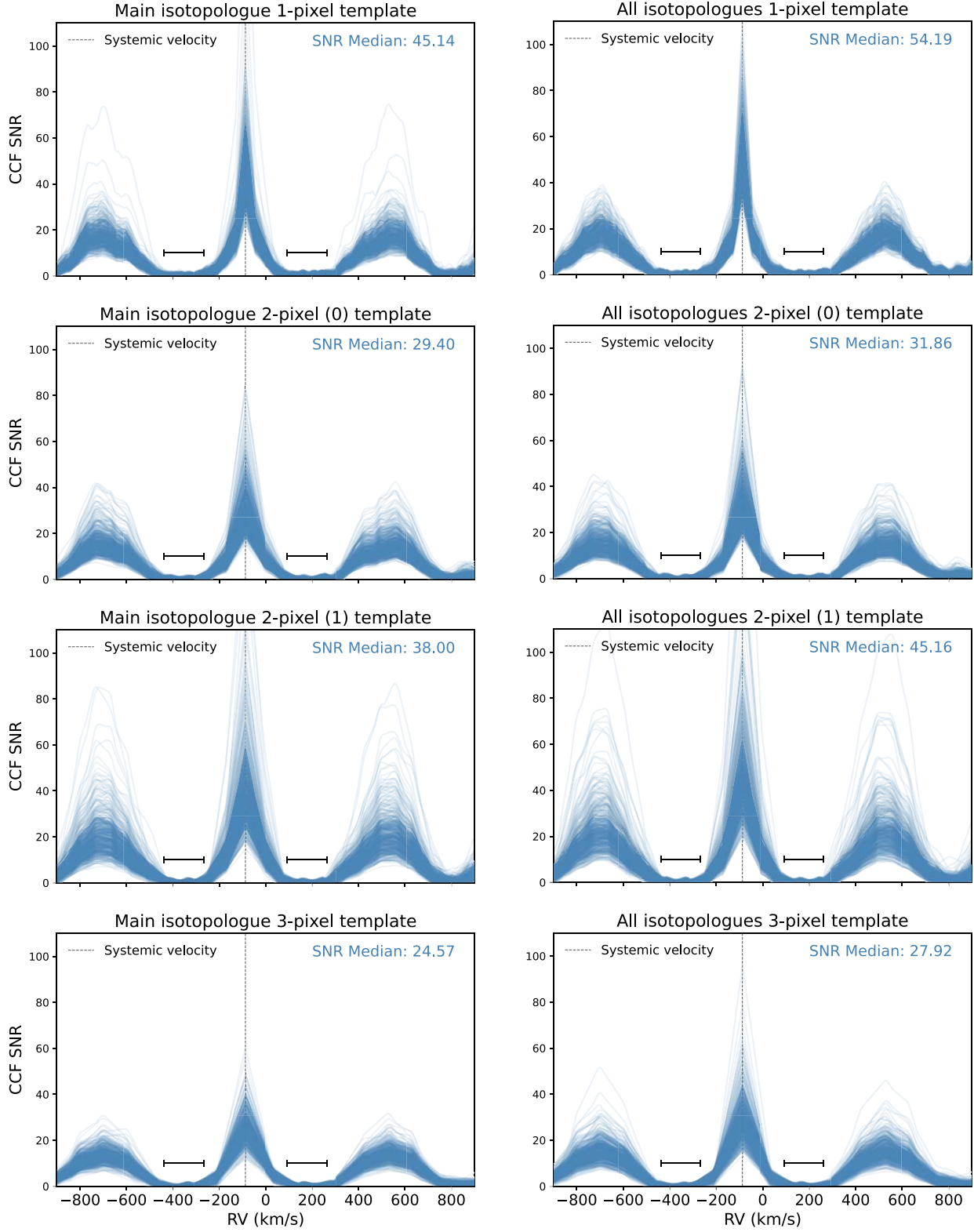


Figure 5. Cross-correlation functions (CCFs) resulting from the cross-correlation of the synthetic transmission spectra with the CO main-isotopologue (left panels) and the CO all-isotopologues templates (right panels) in the 4.6–5.0 μm range using a radial velocity step of 6 km s^{-1} . The first row panels show the resulting CCFs for the 1 pixel sampled transmission spectrum. The second and third rows panels show the resulting CCFs for the 2 pixel sampled transmission spectra, starting in the first and second pixel, respectively. The third row panels show the resulting CCFs for the 3 pixel sampled transmission spectrum. The black horizontal bars indicate the continuum regions used to calculate the signal-to-noise ratio of the CCF, and calculate the significance of the central peak. The black dashed line shows the systemic velocity relative to the JWST at the time of the observation. Additionally, the median signal-to-noise ratio value of the main peak is printed in each panel.

Appendix C $^{12}\text{C}^{16}\text{O} + ^{13}\text{C}^{16}\text{O}$ Cross-correlation Results

We performed an additional cross-correlation analysis of the observed transmission spectrum using a template composed of the two most abundant CO isotopologues: $^{12}\text{C}^{16}\text{O}$ and $^{13}\text{C}^{16}\text{O}$. We generated the template following the procedure detailed in Section 3, setting the relative abundances of the isotopologues to match those of Earth, i.e., 98.7% $^{12}\text{C}^{16}\text{O}$ and 1.3% $^{13}\text{C}^{16}\text{O}$.

Figure 6 shows the model spectrum used as template in this case. The CCF results, shown in Figure 7, are similar to the ones obtained using the CO all-isotopologues template. The significance of the detection, being $7.33_{-1.04}^{+2.26}$ sigma, increases compared to the CO main-isotopologues result but is slightly below the all-isotopologues significance, indicating that the all-isotopologues template produces a better match.

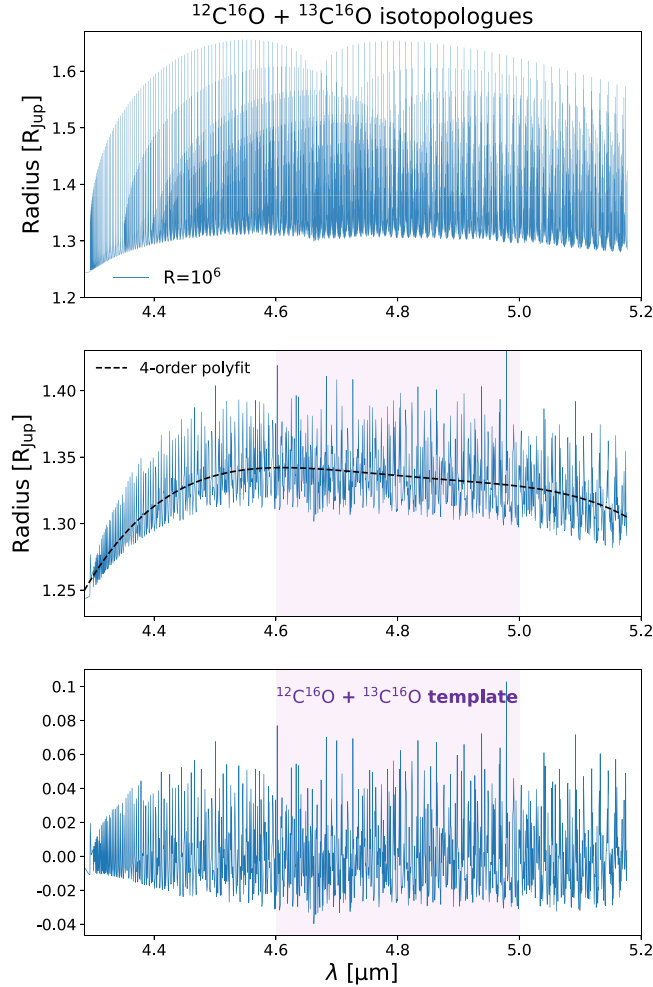


Figure 6. Atmospheric models for the combination of $^{12}\text{C}^{16}\text{O}$ (98.7%) and $^{13}\text{C}^{16}\text{O}$ (1.3%). Top: high-resolution (10^6) petitRADTRANS-computed transmission spectrum model. Middle: CO spectrum model degraded to match the sampling of the observed transmission spectrum. The region used for the cross-correlation search is highlighted in purple. The black dashed line shows the fourth-order polynomial fit that is used for the normalization. Bottom: normalized CO template used in the cross-correlation analysis.

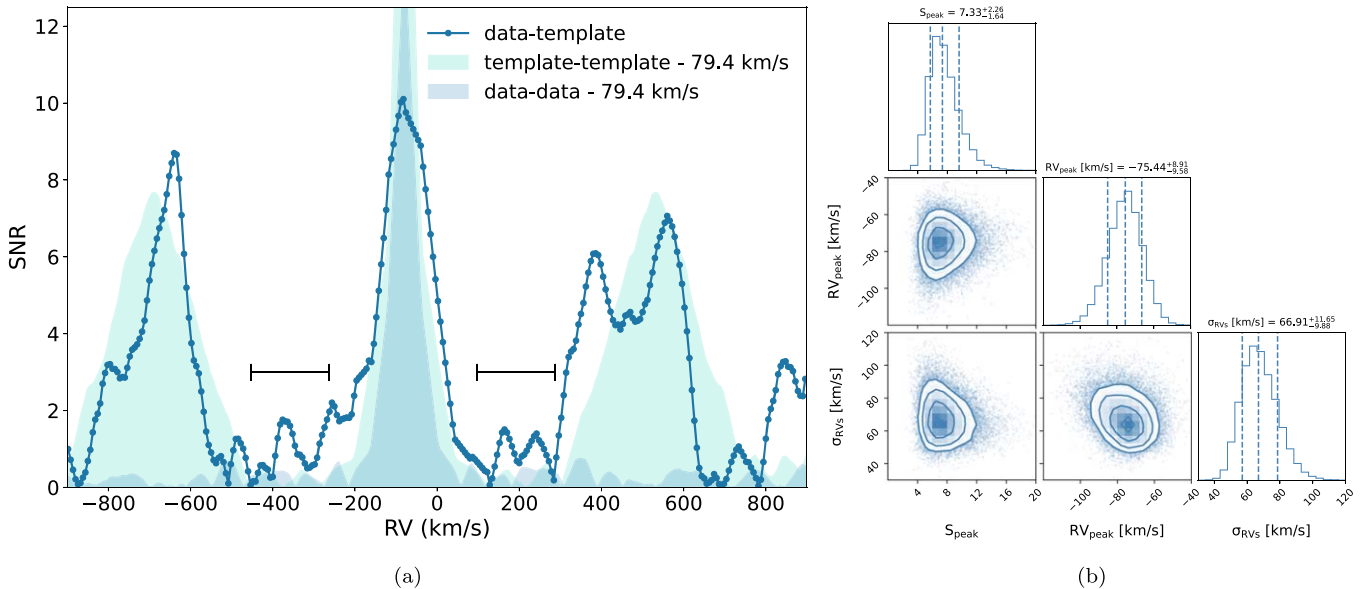


Figure 7. (a) Cross-correlation function (CCF) of the WASP-39b transmission spectrum with the $^{12}\text{C}^{16}\text{O}$ (98.7%) + $^{13}\text{C}^{16}\text{O}$ (1.3%) template. We compare the CCFs resulting from the self cross-correlation of the template (light blue area) and the spectrum (dark blue area), which were scaled arbitrarily. (b) Distribution of the best-fit Gaussian parameters (significance of the central peak, S_{peak} , the central peak velocity, RV_{peak} , and the FWHM of the distribution of velocities, σ_{RVs}) retrieved from the sampled transmission spectra that were randomly generated following a Gaussian distribution centered in the observed transmission spectrum and considering the errors as the Gaussian standard deviation in each point. We performed 30,000 iterations.

ORCID iDs

Emma Esparza-Borges <https://orcid.org/0000-0002-2341-3233>
 Mercedes López-Morales <https://orcid.org/0000-0003-3204-8183>
 Jéa I. Adams Redai <https://orcid.org/0000-0002-4489-3168>
 Enric Pallé <https://orcid.org/0000-0003-0987-1593>
 James Kirk <https://orcid.org/0000-0002-4207-6615>
 Núria Casasayas-Barris <https://orcid.org/0000-0002-2891-8222>
 Natasha E. Batalha <https://orcid.org/0000-0003-1240-6844>
 Benjamin V. Rackham <https://orcid.org/0000-0002-3627-1676>
 Jacob L. Bean <https://orcid.org/0000-0003-4733-6532>
 S. L. Casewell <https://orcid.org/0000-0003-2478-0120>
 Leen Decin <https://orcid.org/0000-0002-5342-8612>
 Leonardo A. Dos Santos <https://orcid.org/0000-0002-2248-3838>
 Antonio García Muñoz <https://orcid.org/0000-0003-1756-4825>
 Joseph Harrington <https://orcid.org/0000-0002-8955-8531>
 Kevin Heng <https://orcid.org/0000-0003-1907-5910>
 Renyu Hu <https://orcid.org/0000-0003-2215-8485>
 Luigi Mancini <https://orcid.org/0000-0002-9428-8732>
 Karan Molaverdikhani <https://orcid.org/0000-0002-0502-0428>
 Giuseppe Morello <https://orcid.org/0000-0002-4262-5661>
 Nikolay K. Nikolov <https://orcid.org/0000-0002-6500-3574>
 Matthew C. Nixon <https://orcid.org/0000-0001-8236-5553>
 Seth Redfield <https://orcid.org/0000-0003-3786-3486>
 Kevin B. Stevenson <https://orcid.org/0000-0002-7352-7941>
 Hannah R. Wakeford <https://orcid.org/0000-0003-4328-3867>
 Munazza K. Alam <https://orcid.org/0000-0003-4157-832X>
 Björn Benneke <https://orcid.org/0000-0001-5578-1498>
 Jasmina Blecic <https://orcid.org/0000-0002-0769-9614>

Nicolas Crouzet [https://orcid.org/0000-0001-7866-8738
 Tansu Daylan \[https://orcid.org/0000-0002-6939-9211
 Julie Inglis \\[https://orcid.org/0000-0001-9164-7966
 Laura Kreidberg \\\[https://orcid.org/0000-0003-0514-1147
 Dominique J. M. Petit dit de la Roche \\\\[https://orcid.org/0000-0002-8963-3810
 Jake D. Turner <https://orcid.org/0000-0001-7836-1787>\\\\]\\\\(https://orcid.org/0000-0002-8963-3810\\\\)\\\]\\\(https://orcid.org/0000-0003-0514-1147\\\)\\]\\(https://orcid.org/0000-0001-9164-7966\\)\]\(https://orcid.org/0000-0002-6939-9211\)](https://orcid.org/0000-0001-7866-8738)

References

- Ahrer, E.-M., Stevenson, K. B., Mansfield, M., et al. 2023, *Natur*, **614**, 653
 Alderson, L., Wakeford, H. R., Alam, M. K., et al. 2023, *Natur*, **614**, 664
 Ambikasaran, S., Foreman-Mackey, D., Greengard, L., Hogg, D. W., & O’Neil, M. 2015, *ITPAM*, **38**, 252
 Barman, T. S., Konopacky, Q. M., Macintosh, B., & Marois, C. 2015, *ApJ*, **804**, 61
 Bean, J. L., Stevenson, K. B., Batalha, N. M., et al. 2018, *PASP*, **130**, 114402
 Benneke, B., Wong, I., Piaulet, C., et al. 2019, *ApJL*, **887**, L14
 Birkmann, S. M., Ferruit, P., Giardino, G., et al. 2022, *A&A*, **661**, A83
 Brogi, M., de Kok, R. J., Birkby, J. L., Schwarz, H., & Snellen, I. A. G. 2014, *A&A*, **565**, A124
 Brogi, M., Snellen, I. A. G., de Kok, R. J., et al. 2012, *Natur*, **486**, 502
 Carnall, A. C. 2017, arXiv:[1705.05165](https://arxiv.org/abs/1705.05165)
 Clayton, D. D., & Nittler, L. R. 2004, *ARA&A*, **42**, 39
 Cridland, A. J., van Dishoeck, E. F., Alessi, M., & Pudritz, R. E. 2019, *A&A*, **632**, A63
 Crouzet, N., McCullough, P. R., Deming, D., & Madhusudhan, N. 2014, *ApJ*, **795**, 166
 Czesla, S., Schröter, S., Schneider, C. P., et al. 2019, PyA: Python astronomy-related packages, Astrophysics Source Code Library, ascl:[1906.010](https://ascl.net/1906.010)
 de Kok, R. J., Brogi, M., Snellen, I. A. G., et al. 2013, *A&A*, **554**, A82
 Deming, D., & Sheppard, K. 2017, *ApJL*, **841**, L3
 Deming, D., Wilkins, A., McCullough, P., et al. 2013, *ApJ*, **774**, 95
 Faedi, F., Barros, S. C. C., Anderson, D. R., et al. 2011, *A&A*, **531**, A40
 Feinstein, A. D., Radica, M., Welbanks, L., et al. 2023, *Natur*, **614**, 670
 Foreman-Mackey, D., Hogg, D. W., Lang, D., & Goodman, J. 2013, *PASP*, **125**, 306
 Grant, D., & Wakeford, H. R. 2022, Exo-TiC/ExoTiC-LD: ExoTiC-LD v3.0.0, Zenodo, doi:[10.5281/zenodo.7437681](https://doi.org/10.5281/zenodo.7437681)
 Grant, D., Lothringer, J. D., Wakeford, H. R., et al. 2023, *ApJL*, **949**, L15
 Jakobsen, P., Ferruit, P., Alves de Oliveira, C., et al. 2022, *A&A*, **661**, A80

- JWST Transiting Exoplanet Community Early Release Science, Ahrer, E. M., Alderson, L., et al. 2023, *Natur*, **614**, 649
- Kirk, J., López-Morales, M., Wheatley, P. J., et al. 2019, *AJ*, **158**, 144
- Kirk, J., Wheatley, P. J., Louden, T., et al. 2017, *MNRAS*, **468**, 3907
- Kirk, J., Wheatley, P. J., Louden, T., et al. 2018, *MNRAS*, **474**, 876
- Kirk, J., Rackham, B. V., MacDonald, R. J., et al. 2021, *AJ*, **162**, 34
- Konopacky, Q. M., Barman, T. S., Macintosh, B. A., & Marois, C. 2013, *Sci*, **339**, 1398
- Kreidberg, L. 2015, *PASP*, **127**, 1161
- Madhusudhan, N., Bitsch, B., Johansen, A., & Eriksson, L. 2017, *MNRAS*, **469**, 4102
- Mancini, L., Esposito, M., Covino, E., et al. 2018, *A&A*, **613**, A41
- Miles, B. E., Biller, B. A., Patapis, P., et al. 2023, *ApJL*, **946**, L6
- Mollière, P., & Snellen, I. A. G. 2019, *A&A*, **622**, A139
- Mollière, P., Wardenier, J. P., van Boekel, R., et al. 2019, *A&A*, **627**, A67
- Mordasini, C., van Boekel, R., Mollière, P., Henning, T., & Benneke, B. 2016, *ApJ*, **832**, 41
- Öberg, K. I., Murray-Clay, R., & Bergin, E. A. 2011, *ApJL*, **743**, L16
- Petit dit de la Roche, D. J. M., Hoeijmakers, H. J., & Snellen, I. A. G. 2018, *A&A*, **616**, A146
- Rigby, J., Perrin, M., McElwain, M., et al. 2023, *PASP*, **135**, 048001
- Rodler, F., Lopez-Morales, M., & Ribas, I. 2012, *ApJL*, **753**, L25
- Rothman, L. S., Gordon, I. E., Barber, R. J., et al. 2010, *JQSRT*, **111**, 2139
- Rustamkulov, Z., Sing, D. K., Mukherjee, S., et al. 2023, *Natur*, **614**, 659
- Snellen, I. A. G., de Kok, R. J., de Mooij, E. J. W., & Albrecht, S. 2010, *Natur*, **465**, 1049
- Stevenson, K., Agol, E., Angerhausen, D., et al. 2016, A Preparatory Program to Identify the Single Best Transiting Exoplanet for JWST Early Release Science, HST Proposal, Cycle 24, #14642
- Tonry, J., & Davis, M. 1979, *AJ*, **84**, 1511
- Tsai, S. M., Lee, E. K. H., Powell, D., et al. 2023, *Natur*, **617**, 483
- van Sluijs, L., Birkby, J. L., Lothringer, J., et al. 2023, *MNRAS*, **522**, 2145
- Virtanen, P., Gommers, R., Oliphant, T. E., et al. 2020, *NatMe*, **17**, 261
- Wakeford, H. R., Sing, D. K., Deming, D., et al. 2018, *AJ*, **155**, 29
- Zhang, Y., Snellen, I. A. G., & Mollière, P. 2021a, *A&A*, **656**, A76
- Zhang, Y., Snellen, I. A. G., Bohn, A. J., et al. 2021b, *Natur*, **595**, 370